Sensitivity of seafloor bathymetry to climate-driven fluctuations in mid-ocean ridge magma supply

J. -A. Olive[1]*, M. D. Behn[2], G. Ito[3], W. R. Buck[1], J. Escartin[4], S. Howell[3]

[1]Lamont-Doherty Earth Observatory / Columbia University, Palisades NY, USA.

[2]Woods Hole Oceanographic Institution, Woods Hole MA, USA.

[3]University of Hawaii, Honolulu HI, USA.

[4]CNRS / Institut de Physique du Globe de Paris, Paris, France.

*Correspondence to: J. -A. Olive, jaolive@ldeo.columbia.edu

Abstract: **Recent studies have proposed that the bathymetric fabric of the seafloor formed at mid-ocean ridges records rapid (23–100 kyr) fluctuations in ridge magma supply caused by sea level changes that modulate melt production in the underlying mantle. Using quantitative models of faulting and magma emplacement, we demonstrate that, in fact, seafloor-shaping processes act as a low-pass filter on variations in magma supply, strongly damping fluctuations shorter than ~100 kyr. We show that the systematic decrease in dominant seafloor wavelengths with increasing spreading rate is best explained by a model of fault growth and abandonment under a steady magma input. This provides a robust framework for deciphering the footprint of mantle melting in the fabric of abyssal hills, the most common topographic feature on Earth.**

One Sentence Summary: The fabric of the seafloor is best explained by the interaction between fault growth and crustal emplacement, which is largely insensitive to climatically controlled variations in ridge magma supply.

Main Text: Seafloor abyssal hills are the most common topographic feature on the surface of the solid Earth. They consist of a juxtaposition of bathymetric highs and lows with a characteristic spacing of 1–10 km and amplitude of up to a few hundred meters, elongated parallel to crustal isochrons (*1*-*3*). These features form at mid-ocean ridges (MORs) through the interaction of volcanism and faulting coincident with the creation of new oceanic lithosphere (*2*, *4*, *5*) (Fig. 1).

The fabric of abyssal hills has recently been proposed to record fluctuations in MOR magma supply driven by climatically controlled sea level variations with a periodicity of up to 100 kyr (*6*). It was shown that sea level changes of ~100 m associated with glacial (Milankovitch) cycles could induce pressure changes on the sub-ridge mantle undergoing decompression melting, thereby modulating the flux of melt supplied to the ridge axis (*6*, *7*). This mechanism was proposed to drive oceanic crustal thickness fluctuations of ~600 m, and give rise to isostatically compensated seafloor topography with wavelengths reflecting Milankovitch periodicities (23, 41, and 100 kyr). Spectral power at these wavelengths in the bathymetry of the intermediate-spreading Australian-Antarctic Ridge (AAR) was presented as evidence for this process (*6*). Moreover, an independent study revealed a strong spectral peak near the 100-kyr period for seafloor created at the fast-spreading East Pacific Rise, although

peaks at the 23- and 41-kyr periods were not observed (*8*). If confirmed, a major implication of this model is that abyssal hill fabric represents a proxy for paleo sea level change.

Climate-driven changes in magma supply in several terrestrial settings have been attributed to the loss of glaciers, some up to 2 km thick (*9*, *10*). However, whether ~100 m change in sea level can be effectively recorded in seafloor bathymetry is unclear (*6*, *7*, *11*). We combine classic seafloor observations with recently developed and improved models of MOR dynamics to determine whether oscillations in melt supply of a given period (τ) can imprint seafloor bathymetry through three mechanisms: (I) static topographic compensation, (II) volcanic extrusion on the seafloor, and (III) tectono-magmatic interactions during normal fault growth.

The first mechanism linking MOR magma supply and seafloor bathymetry is (I) temporal (and hence cross-axis) oscillations in crustal thickness applying a vertical load on the oceanic lithosphere that can deflect the seafloor (*6*). The wavelength of the load ($U \cdot \tau$, where U is the spreading half-rate) strongly controls the response of the lithosphere, which is commonly described as the flexing of a thin elastic plate of effective thickness T_e (*12*, *13*) (Fig. 2A). Because ~70% of the entire crust at intermediate- and fast-spreading ridges accretes as intrusive lower crust (*14*), fluctuations in melt supply will be expressed primarily as vertical undulations of the crust-mantle interface loading the lithosphere from below. In ref. *6*, however, flexure was ignored in favor of an Airy isostasy approximation. This yielded variations in seafloor topography of ~150 m in response to 600 m variations in crustal thickness driven by sea level changes over a range of spreading rates. This approximation is valid when $U \cdot \tau$ is greater than ~100 T_e, but this is not likely to be the case in general.

At slow-spreading ridges, Milankovitch cycles would create crustal loads of wavelength < 3 km, which is considerably less than 10 T_e, as T_e has been shown to be greater than ~1 km (*13*, *15*). Such loads should result in essentially no seafloor topography (Fig. 2A). By contrast, T_e is likely to be minimal at fast-spreading ridges, such as the East Pacific Rise, where the observed rise crest topography is best explained by a T_e of 100 m at the axis, though it thickens rapidly with lithosphere age to reach ~800 m in 100 kyr old lithosphere (*16*). A value of T_e = 100 m could explain topographic variations of ~70–110 m at the wavelength corresponding to the longest Milankovitch period (i.e., 8 km for U = 8 cm/yr, assuming average crustal densities between 2850 and 3000 kg.m^{-3}). However, this estimate drops to ~5 m when using a value of T_e averaged over the wavelength of the load (T_e = 500 m) (Fig. 2A). Finally, at the AAR (U = 3 cm/yr), creating seafloor topography greater than 10 m would require a $T_e \leq 100$ m, unrealistically low for an intermediate-spreading ridge. In short, the lithosphere most often constitutes a strong topographic filter to such short wavelength oscillations in crustal thickness.

Yet, another consideration suggests that a ~600 m variation in crustal thickness is an overestimate. Namely, magma arising out of the mantle is delivered to a magma storage (accretion) region of finite-width within the crust, prior to solidifying in a neovolcanic zone of comparable width (*17*, *18*) (Fig. 1). If the melt input (volume per unit time per unit length of ridge) fluctuates by an amount $\Delta\Phi_0$ on a period shorter than its characteristic residence time in the accretion zone, these oscillations will generate crustal thickness variations that are reduced compared to estimates that assume an infinitesimally narrow accretion zone ($\Delta h_0 = \Delta\Phi_0 / 2U \sim$ 600 m as in ref. *6*). For example, simple mass balance arguments (*12*) predict that an intermediate spreading ridge such as the AAR with a characteristic accretion zone width of 1 km would more realistically produce crustal thickness oscillations of ~410, 220, and 120 m on Milankovitch periods of 100, 41, and 23 kyr, respectively (Fig. 2B). But again at slow-to-

intermediate spreading rates, lithospheric flexure should drastically impede any topographic expression of these reduced thickness oscillations. At the fast-spreading East Pacific Rise (U = 8 cm/yr) seismic evidence points to a characteristic accretion width of ~5 km (*19*). This would reduce both the estimated 100-kyr crustal thickness variation and its topographic expression by a factor of 0.45, enabling at most 30–50 m of topography for the lowest estimate of lithospheric strength (T_e = 100 m).

The second mechanism for generating topography in response to oscillations in magma supply considers (II) the portion added to the extrusive upper crust. The time-averaged volume of extruded material is thought to reflect the overpressure in an axial melt lens pushing magma upwards to the seafloor (*20*). When transitioning from a period of thin to thick axial crust due to a change in melt supply, the overpressure must increase to compensate the replacement of dense mantle by lighter lower crust. This assumption (*12*) is different from that of isostatic or flexural equilibrium explored earlier, as a column of magma rising to the surface is mechanically decoupled from the rest of the lithosphere. We can use it to estimate the thickness variation of the extrusive portion of the crust Δh_{UC} that results from the crustal thickness variations Δh = 410, 220, 120 m expected at the AAR (Fig. 2B). This yields Δh_{UC} = 60–85, 33–46, and 18–25 m, respectively, depending on the density assumed for the oceanic crust. A similar reasoning predicts topographic fluctuations of 40–55 m on a 100-kyr period at the East Pacific Rise. They are, however, unlikely to strongly overprint the tectonic fabric of the seafloor, which typically consists of fault scarps greater than 200 m at slow and intermediate-spreading ridges (*3*), and about 50–100 m at fast-spreading ridges (*21*). Moreover, these amplitudes are probably upper bounds, as seafloor eruptions involve lava flows spreading up to a few km in the cross-axis direction (*22*), providing another topographic damping process.

An important corollary to both of the above mechanisms (I and II) is that the wavelength of the sea level-modulated topography should increase in proportion to spreading rate. However, the spacing of abyssal hills, which constitutes the dominant wavelength in the spectrum of the seafloor (*23*), is observed to decrease with increasing spreading rate from ~10 km at slow-spreading ridges down to ~2 km at fast-spreading ridges (Fig. 3A). Thus, any viable model for abyssal hill formation must explain this global trend.

Given that abyssal hills are typically bounded by major normal faults (*2*), we favor an alternative model in which the decrease in abyssal hill spacing reflects the increasing importance of magmatically versus tectonically accommodated extension at faster-spreading ridges (*24*). With this framework, we explore the possibility that (III) a fluctuating magma supply influences the pattern of faulting, which shapes the seafloor fabric.

In a time-averaged sense, dike intrusion in the axial lithosphere accommodates a fraction M of the total plate separation (Fig. 3B). The remaining fraction (1–M) is accommodated by slip on normal faults that initiate near the axis, and are subsequently pushed off-axis by magmatic intrusion at a rate that increases with M (*24, 25*). As a fault encounters progressively thicker off-axis lithosphere, the work required to keep it active increases until it becomes mechanically favorable to abandon it in favor of a new fault forming closer to the axis (Fig. 3B). Mechanical scaling laws (*12*) predict that thick or rapidly thickening lithosphere with a robust magma supply (high M) produces relatively short-lived, and therefore closely spaced faults (*24*, *25*). Upon parameterizing axial lithospheric thickness, thickening rate, and M, vs. spreading rate through empirical fits to observations (inset in Fig. 3A, Fig. S2), we use these mechanical scaling laws to predict a decrease in abyssal hill spacing from ~10 to ~2.5 km with increasing spreading rate, following the trend of the observations (Fig. 3A). Thus, the systematic variations in abyssal hill

fabric with spreading rate are best explained by a model of tectono-magmatic extension under a steady magma input.

Steady magma input is an oversimplification of the ridge magmatic system, even without climatic variations in magma flux (*26*, *27*). Thus, we consider the possibility that an oscillating magma input could alter the above behavior by directly impacting the duration that individual faults remain active (*28*), and therefore imprint the seafloor fabric. We performed 2-D numerical simulations of normal fault growth coupled with magmatic injection in the lithosphere that fluctuates on a period τ (*12*). During 85% of the cycle, magma injection accommodates 100% of plate separation (U = 3 cm/yr), whereas during the remaining 15% extension is fully accommodated on faults that form spontaneously in the lithosphere. This scenario maximizes the effects of magmatic modulation, but has a time-averaged M equal to 0.85 (*28*).

We ran 12 simulations with τ ranging from 10 to 500 kyr. The modeled seafloor shows abyssal hill-like topography, from which we measure the mean fault spacing (Fig. 4A). The spectrum of topography clearly shows that fault spacing expresses a dominant wavelength (Fig. 4B). It also reveals a number of peaks at higher wavenumbers (within the Milankovitch range) that cannot be directly interpreted in terms of seafloor length scales. Simulations with short τ consistently produce abyssal hills with a characteristic spacing of ~2–4 km, as predicted by the mechanical scaling laws that assume a steady magma input (horizontal red line in Fig. 4C). Simulations with a longer τ, however, reveal a direct control of the forcing period on fault spacing (blue curve). The transition between the two regimes occurs at a period set by the mechanically controlled fault spacing divided by the spreading half-rate, which at intermediate-spreading ridges is ~100 kyr. We therefore expect the tectonic fabric of the AAR to be insensitive to even extreme fluctuations in melt supply on Milankovitch frequencies. The spectral peaks observed there (*6*) likely reflect only the mechanically controlled spacing of fault-bounded abyssal hills as shaped by the time-averaged melt supply ($M \sim 0.85$) (Fig. 3A, 4B).

Each of the three mechanisms of topography development acts as a low-pass filter of melt supply with strong damping of periods shorter than ~100 kyr. Therefore, the fingerprints of a climate modulation in MOR melt supply may be found more easily through multichannel seismic imaging of the crust-mantle boundary than through bathymetric analysis. If short-wavelength topography on the base of the crust is observed, comparing its spectral characteristics in crust younger and older than the onset of pronounced glacial cycles would provide a valuable test of the predictions made here and by earlier studies (*6-8*).

References and Notes:

1. H. Menard, J. Mammerickz, Abyssal hills, magnetic anomalies and the East Pacific Rise, *Earth Planet. Sci. Lett.*, **2**, 465-472 (1967).

2. K. C. Macdonald, P. J. Fox, R. T. Alexander, R. Pockalny, P. Gente, Volcanic growth faults and the origin of Pacific abyssal hills, *Nature*, **380**, 125-129 (1996).

3. J. A. Goff, Y. Ma, A. Shah, J. R. Cochran, J. -C. Sempéré, Stochastic analysis of seafloor morphology on the flank of the Southeast Indian Ridge: The influence of ridge morphology on the formation of abyssal hills, *J. Geophys. Res.*, **102** (B7), 15521-15534 (1997).

4. D. K. Rea, Model for the formation of topographic features on the East Pacific Rise crest, *Geology*, **3**, 77-80 (1975).

5. E. S. Kappel, W. B. F. Ryan, Volcanic episodicity and a non-steady state rift valley along Northeast Pacific spreading centers: Evidence from Sea MARC I, *J. Geophys. Res.*, **91**, 13925-13940 (1986).

6. J. W. Crowley, R. F. Katz, P. Huybers, C. H. Langmuir, S. H. Park, Glacial cycles drive variations in the production of oceanic crust, *Science*, **347** (6227), 1237-1240 (2015).

7. D. C. Lund, P. D. Asimow, Does sea level influence mid-ocean ridge magmatism on Milankovitch timescales, *Geochem, Geophys. Geosyst.*, **12**, 12009 (2011).

8. M. Tolstoy, Mid-ocean ridge eruptions as a climate valve, *Geophys. Res. Lett.*, **42** (5), 1346-1351 (2015).

9. M. Nakada, H. Yokose, Ice age as a trigger of active Quaternary volcanism and tectonism, *Tectonophysics*, **212**, 321-329 (1992).

10. M. Jull, D. McKenzie, The effect of deglaciation on mantle melting beneath Iceland, *J. Geophys. Res.*, **101** (B10), 21815-21828 (1996).

11. P. J. Huybers, C. H. Langmuir, Feedback between deglaciation, volcanism, and atmospheric CO_2, *Earth Planet. Sci. Lett.*, **286** (3-4), 479-491 (2009).

12. Materials and methods are available as supplementary materials on Science Online.

13. A. B. Watts, *Isostasy and flexure of the lithosphere* (Cambridge Univ. Press, Cambridge, UK, 2001).

14. J. Phipps Morgan, Y. J. Chen, The genesis of oceanic crust: Magma injection, hydrothermal circulation, and crustal flow, *J. Geophys. Res.*, **98** (B4), 6283–6297 (1993).

15. J. R. Cochran, An analysis of isostasy in the world's oceans 2. Mid-ocean ridge crests, *J. Geophys. Res.*, **84** (B9) (1979).

16. B. -Y. Kuo, D. W. Forsyth, E. M. Parmentier, Flexure and thickening of the lithosphere at the East Pacific Rise , *Geophys. Res. Lett.*, **13**, 681-684 (1986).

17. J. M. Sinton, R. S. Detrick, Mid-ocean ridge magma chambers, *J. Geophys. Res.*, **97**, 197-216 (1992).

18. M. R. Perfit, W. W. J. Chadwick, in *Faulting and Magmatism at Mid-Ocean Ridges*, W. R. Buck *et al.* Eds. (AGU, Washington DC, 1998) pp. 59-115.

19. R. A. Dunn, D. R. Toomey, Seismological evidence for three-dimensional melt migration beneath the East Pacific Rise, *Nature*, **388**, 259-262 (1997).

20. W. R. Buck, S. M. Carbotte, S., C. Z. Muiter, Controls on extrusion at mid-ocean ridges, *Geology*, **25**, 935-938 (1997).

21. S. M. Carbotte, K. C. Macdonald, Comparison of sea floor tectonic fabric created at intermediate, fast and super fast spreading ridges: Influence of spreading rate, plate motions, and ridge segmentation on fault patterns, *J. Geophys. Res.,* **99**, 13609-13633 (1994).

22. J. Escartín *et al.*, Interplay between faults and lava flows in construction of the upper oceanic crust: The East Pacific Rise crest 9º25' - 9º58'N, *Geochem. Geophys. Geosyst.*, **8**, Q06005 (2007).

23. J. A. Goff, T. H. Jordan, Stochastic modeling of seafloor morphology: Inversion of sea beam data for second-order statistics, *J. Geophys. Res.*, **93** (B11), 13589-13608 (1988).

24. W. R. Buck, L. L. Lavier, A. N. B. Poliakov, Modes of faulting at mid-ocean ridges, *Nature*, **434**, 719-723 (2005).

25. M. D. Behn, G. Ito, Magmatic and tectonic extension at mid-ocean ridges: 1. Controls on fault characteristics, *Geochem. Geophys. Geosyst.*, **9** (8), Q08O10 (2008).

26. J. P. Canales, J. A. Collins, J. Escartín, R. S. Detrick, Seismic structure across the rift valley of the Mid-Atlantic Ridge at 23º20' (MARK area): Implications for crustal accretion processes at slow-spreading ridges, *J. Geophys. Res.*, **105** (B12), 28411-28425 (2000).

27. E. Bonatti *et al.*, Mantle thermal pulses below the Mid-Atlantic Ridge and temporal variations in the formation of oceanic lithosphere, *Nature*, **423**, 499-505 (2003).

28. G. Ito, M. D. Behn, Magmatic and tectonic extension at mid-ocean ridges: 2. Origin of axial morphology, *Geochem, Geophys. Geosyst.*, **9**, Q08O10 (2008).

29. J. Karsten *et al.* (1999), The northern Chile Ridge revealed: Preliminary cruise report of PANORAMA Expedition Leg 04, *Intern. Ridge-Crest Res.*, **8** (1), 15-21 (1999).

30. A. Malinverno, R. A. Pockalny, Abyssal hill topography as an indicator of episodicity in crustal accretion and deformation , *Earth Planet. Sci. Lett.*, **99**, 154-169 (1990).

31. P. A. Cowie, A. Malinverno, W. B. F. Ryan, M. H. Edwards, Quantitative Fault Studies on the East Pacific Rise: A Comparison of Sonar Imaging Techniques, *J. Geophys. Res.,* **99**, 15205-15218 (1994).

32. A. Macario *et al.*, Flow line variations in abyssal hill morphology for the Pacific-Antarctic Ridge at 65ºS, *J. Geophys. Res.*, **99**, 17921-17934 (1994).

33. J. Escartín *et al.*, Quantifying tectonic strain and magmatic accretion at a slow-spreading ridge-segment (Mid-Atlantic Ridge, 29°N), *J. Geophys. Res.*, **104**, 10421-10437 (1999).

34. D. W. Forsyth, Finite extension and low-angle normal faulting, *Geology*, **20** (1), 27-30 (1992).

35. W. R. Buck, Effect of lithospheric thickness on the formation of high- and low-angle normal faults, *Geology*, **21** (10), 933-936 (1993).

36. L. L. Lavier, W. R. Buck, A. N. B. Poliakov, Factors controlling normal fault offset in an ideal brittle layer, *J. Geophys. Res.*, **105** (B10), 23431-23442 (2000).

37. J. -A. Olive, M. D. Behn, L. C. Malatesta, Modes of extensional faulting controlled by surface processes, *Geophys. Res. Lett.*, **41** (19), 6725-6733 (2014b).

38. J. -A. Olive, M. D. Behn, Rapid rotation of normal faults due to flexural stresses: An explanation for the global distribution of normal fault dips, *J. Geophys. Res.*, **119** (2014).

39. B. E. Tucholke, M. D. Behn, W. R. Buck, J. Lin, Role of melt supply in oceanic detachment faulting and formation of megamullions, *Geology*, **36**, 455-458 (2008).

40. H. Schouten, D. K. Smith, J. R. Cann, J. Escartín, Tectonic versus magmatic extension in the presence of core complexes at slow-spreading ridges from a visualization of faulted seafloor topography, *Geology*, **38** (7), 615-618 (2010).

41. L. G. J. Montési, M. D. Behn, Mantle flow and melting at oblique and ultraslow mid-ocean ridges, *Geophys. Res. Lett.*, **34**, L24307 (2007).

42. P. A. Cundall, Numerical experiments on localization in frictional materials, *Ingenieur Archiv*, **59**, 148-159 (1989).

43. A. N. B. Poliakov, W. R. Buck, in *Faulting and Magmatism at Mid-Ocean Ridges*, W. R. Buck *et al.* Eds. (AGU, Washington DC, 1998) pp. 305-323.

44. S. J. Mackwell, M. E. Zimmerman, D.L. Kohlstedt, High-temperature deformation of dry diabase with application to tectonics on Venus, *J. Geophys. Res.*, **103** (B1), 975-984 (1998).

Acknowledgments: This work greatly benefited from discussions with Pablo Canales, Adam Soule, Suzanne Carbotte, Richard Katz, Peter Huybers, and Bill Ryan, as well as the constructive feedback from three anonymous reviewers. Funding was provided by NSF grants OCE-1154238 (J.-A.O., M.D.B), OCE-1155098 (G.I., S.H.), EAR-1009839 (W.R.B), CNRS support to JE, and an LDEO Postdoctoral Fellowship for J.-A.O. The data and model results presented here are included or fully referenced in the Supplementary Materials.

Supplementary Materials:

Materials and Methods

Figures S1-S2

References (*34-44*)

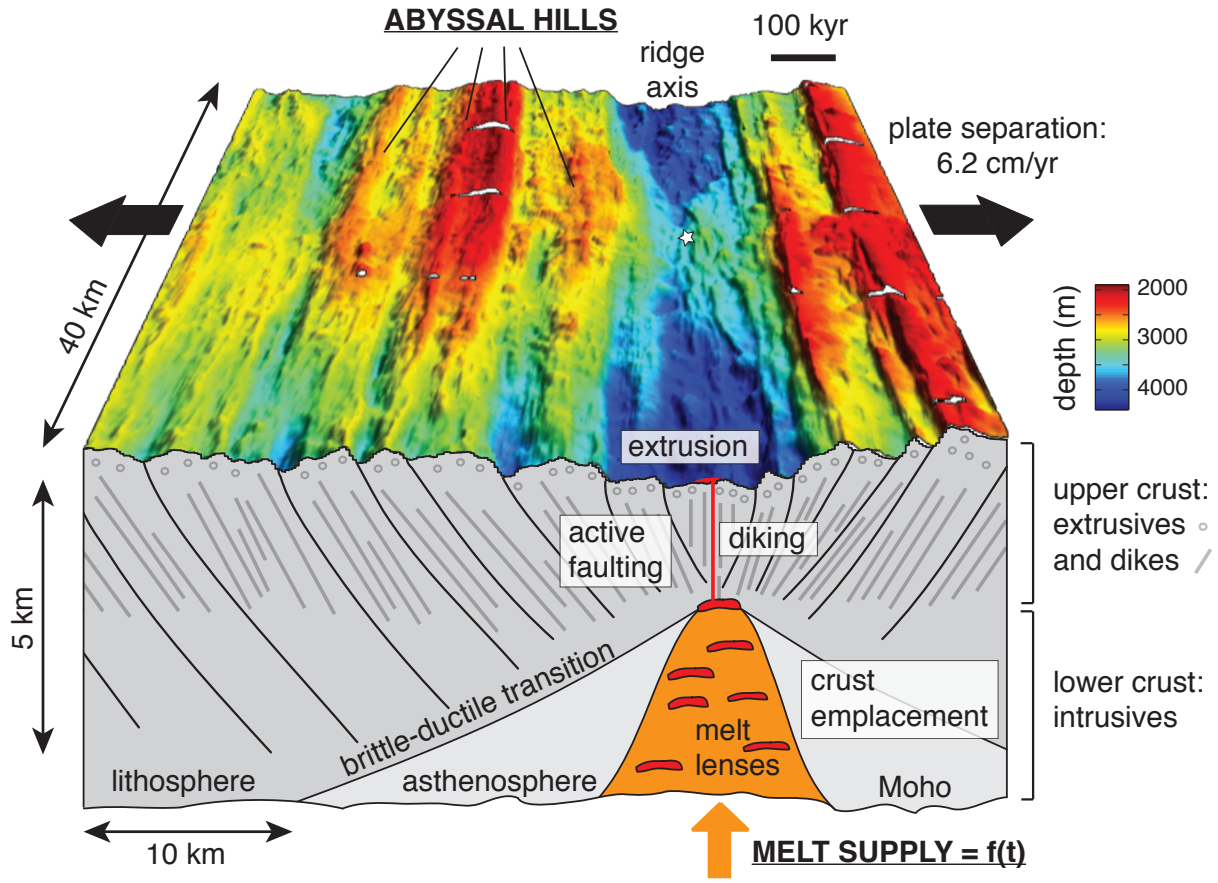

Fig. 1. Abyssal hill fabric formed at the intermediate-spreading Chile Ridge. Bathymetry of a segment of the intermediate-spreading Chile Ridge (*29*) located at 39°12'S, 91°30'W (white star), looking south. Beneath is a schematic cross-section showing the major tectono-magmatic processes that shape the seafloor as melt supplied from below is emplaced as new oceanic crust.

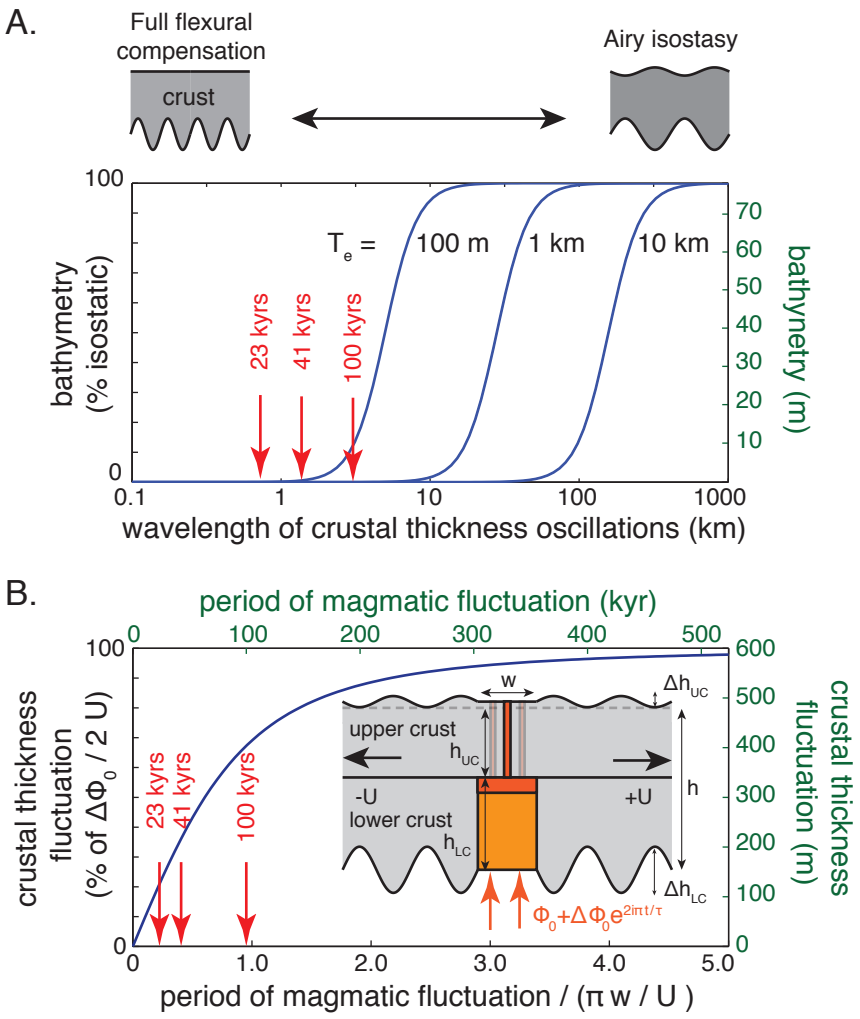

Fig. 2. Seafloor topography from static compensation mechanisms.
(A) Bathymetric relief created in response to oscillations in crustal thickness on a given wavelength, assuming 3 different effective elastic thicknesses (T_e) for the lithosphere. Relief amplitude is given in percent of the isostatic end-member (black axis), and in meters, assuming a crustal thickness fluctuation of 600 m and a density of 3000 kg.m^{-3} for the oceanic crust (green axis). Red arrows indicate the seafloor wavelengths corresponding to Milankovitch periods for a spreading half-rate U = 3 cm/yr. **(B)** Crustal thickness fluctuation ($\Delta h = \Delta h_{UC} + \Delta h_{LC}$) resulting from emplacement of a melt flux oscillating by $\Delta\Phi_0$, within a zone of width w, on a period τ. Green axes (dimensional) illustrate the case where U = 3 cm/yr and w = 1 km. Black axes are normalized.

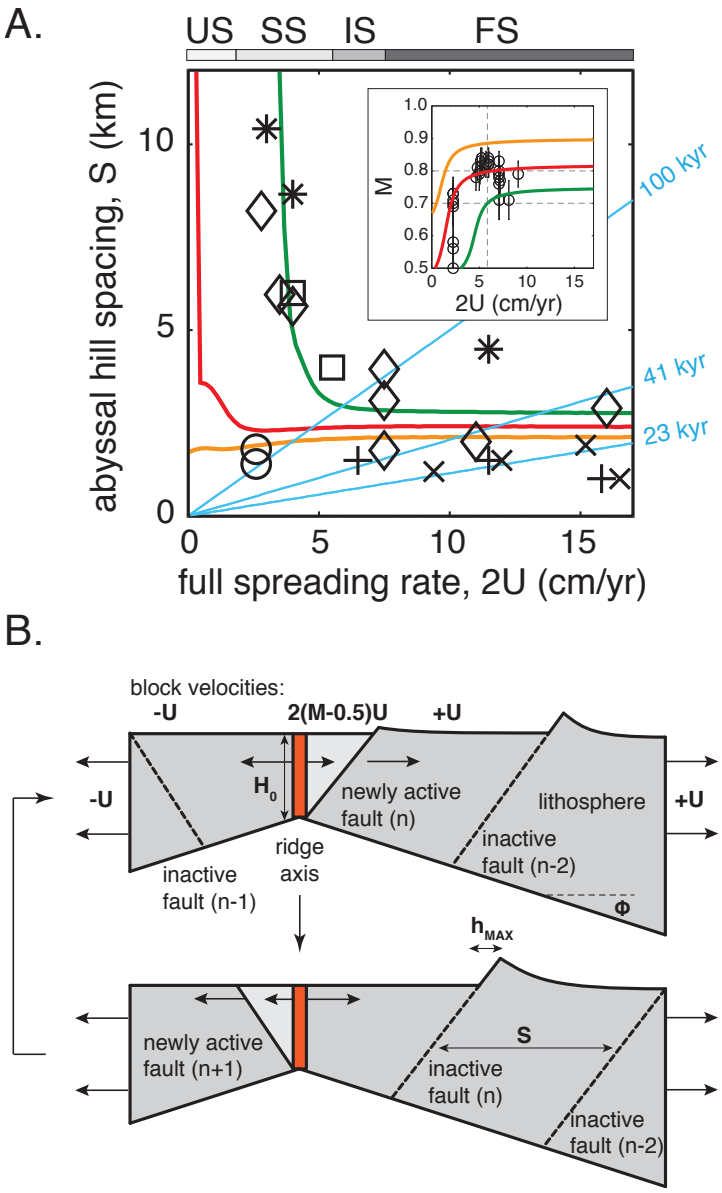

Fig. 3. A tectono-magmatic interaction model for the spacing of abyssal hills
(A) Abyssal hill spacing data obtained from various studies of MOR bathymetry: diamonds (*3*), plus signs (*21*), stars (*30*), crosses (*31*), squares (*32*), and circles (*33*); US, SS, IS, and FS: ultraslow-, slow-, intermediate- and fast-spreading ridges. Green, red, and orange curves show model predictions corresponding to estimates of *M* vs. spreading rate shown as inset, and calibrated on measurements (circles, ref. *25*, with error bars indicating the full range of uncertainty in the determination of *M* from bathymetric profiles). Blue lines illustrate spacing controlled by Milankovitch periods. **(B)** Schematic cross-section showing the basic cycle of fault growth interacting with dike injection at the ridge axis (*12*).

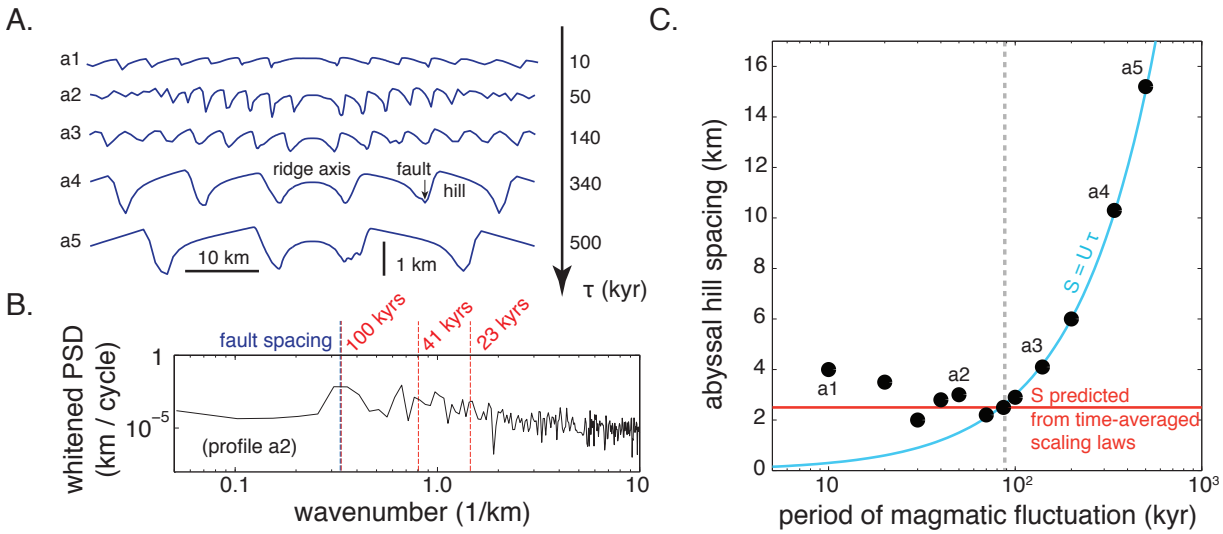

Fig. 4. Sensitivity of MOR bathymetry to fluctuating dike injection rates
(A) Bathymetry obtained from numerical models of sequential faulting interacting with intermittent magma emplacement on an imposed period τ, amounting to a time-averaged M = 0.85 over 1.1 Myr. **(B)** Whitened power spectral density (PSD) of modeled profile a2 (first 20 km to the right of the ridge axis). Blue dashed line shows measured fault spacing, red lines show Milankovitch wavelengths. **(C)** Spacing of modeled faults versus imposed period of magmatic fluctuations. Red and blue lines show the predictions of scaling laws and a linear relation between spacing (S) and τ, respectively.

Supplementary Materials for

Sensitivity of seafloor bathymetry to climate-driven fluctuations in mid-ocean ridge magma supply

J. -A. Olive*, M. D. Behn, G. Ito, W. R. Buck, J. Escartin, S. Howell.

*Correspondence to: jaolive@ldeo.columbia.edu

This PDF file includes:

Materials and Methods

Methods

Here we provide details on each of the models presented in the main text.

Flexural compensation of a fluctuating crustal thickness:

Due to the density contrast between mafic oceanic crust (ρ_c = 2850–3000 kg/m^3) and ultramafic mantle (ρ_m = 3300 kg/m^3), crustal thickness oscillations exert a buoyant load on the base of the oceanic lithosphere at the ridge axis, which may result in seafloor topography. The lithosphere's response to gravitational loads is well accounted for by thin elastic plate models (*13*) which relate seafloor bathymetry ($b(x)$) to crustal thickness variations ($\Delta h(x)$) in the following manner:

$$D\frac{d^4b}{dx^4}+(\rho_m-\rho_w)gb=\Delta h(x)g(\rho_m-\rho_c) \quad . \tag{1}$$

In Equation 1, g denotes the acceleration of gravity, ρ_w = 1000 kg/m^3 is the density of water, and D is the effective flexural rigidity of the lithosphere, which depends on effective elastic thickness T_e and Young's modulus and Poisson's ratio (E and ν) according to

$$D=\frac{ET_e^3}{12(1-\nu^2)} \quad . \tag{2}$$

Upon decomposing the crustal thickness variations into a sum of harmonics, the ratio of topographic amplitude to crustal thickness variations of a given wavelength ($\lambda = U\tau$) is

$$\frac{\|b\|}{\|\Delta h\|}=\frac{g(\rho_m-\rho_c)}{D\left(\frac{2\pi}{\lambda}\right)^4+(\rho_m-\rho_w)g} \quad . \tag{3}$$

This function is plotted in Fig. 2A, assuming realistic elastic properties for the oceanic lithosphere (Young's modulus and Poisson's ratio E = 100 GPa and ν = 0.25, respectively). In the limit where crustal thickness oscillates on very long wavelengths ($\lambda \to +\infty$) the lithosphere responds as if it had no rigidity ($D \to 0$). In this case, termed Airy isostasy, the amplitude of bathymetry is (ρ_m - ρ_c) / (ρ_m - ρ_w) ~ 13–20% of the amplitude of the crustal thickness oscillation. However, fluctuations on wavelengths shorter than ~10 times the effective elastic thickness of the lithosphere produce no sizeable topography.

Filtering of crustal thickness fluctuations due to the finite width of the magmatic emplacement zone:

We assume that the magmatic flux $\Phi(t)$ (volume per unit time per unit length along-axis) to a mid-ocean ridge is emplaced within the crust (thickness $h(t)$) over a zone of cross-axis extent w, constant through time (Fig. 2B). The equation describing the flux balance in and out of this accretion zone is,

$$\frac{d}{dt}(wh) = \Phi - 2Uh \tag{4}$$

Let us assume that a fraction of the total melt flux oscillates on a period τ,

$$\Phi = \Phi_0 + \Delta\Phi_0 e^{2\pi i t/\tau}, \tag{5}$$

where, $i = \sqrt{-1}$. The average thickness of the crust corresponds to the emplacement of the steady portion of the melt flux,

$$h_0 = \frac{\Phi_0}{2U}. \tag{6}$$

Upon plugging the periodic part of Equation 5 into Equation 4, we obtain an equation for the fluctuating part of the crustal thickness $\Delta h(t)$,

$$\frac{d}{dt}(\Delta h) + \frac{2U}{w}\Delta h = \frac{\Delta\Phi_0}{w} e^{2\pi i t/\tau}. \tag{7}$$

It is then readily shown that the amplitude of $\Delta h(t)$ strongly depends on the fluctuation period of the melt flux. A very long period fluctuation results in crustal thickness variations of amplitude

$$\Delta h_0 = \frac{\Delta\Phi_0}{2U}. \tag{8}$$

However, fluctuations on periods shorter than the critical period τ_C result in thickness fluctuations of lesser amplitude,

$$\|\Delta h\| = \frac{\Delta h_0}{\sqrt{1 + \left(\frac{\tau_C}{\tau}\right)^2}}, \tag{9}$$

in which

$$\tau_C = \frac{\pi w}{U}. \tag{10}$$

The corresponding damping function is plotted in Fig. 2B. The approximation of $w = 0$ (or equivalently, $\tau >> \tau_C$) leads to $\|\Delta h\| = \Delta h_0$, which is the solution used in ref. *6*.

Topography from volcanic extrusion:

The thickness of the extrusive layer of the oceanic crust can be directly related to the overall crustal thickness through a pressure balance within and below a dike being emplaced at the ridge axis (*20*). Let us assume that lithostatic pressure stays constant in time at a given compensation depth beneath the axis and below the Moho (cartoon in Fig. 2B). When transitioning from a period of thin to thick axial crust due to a change in melt supply, the pressure in the axial melt lens (AML) must increase to compensate the replacement of dense mantle by lighter crust over a height Δh_{LC}. This change in pressure is $\Delta P = (\rho_m - \rho_c)\, g\, \Delta h_{LC}$, and provides an additional pressure head for extruding volcanic materials further up by Δh_{UC}. A pressure balance in the dike relates Δh_{UC} and Δh_{LC} by

$$\Delta h_{UC} = \frac{\rho_m - \rho_c}{\rho_f - \rho_w}\Delta h_{LC}, \tag{11}$$

where ρ_f = 2700 kg/m^3 is the magma density within the dike. Δh_{UC} can be determined with the added constraint that over many extrusion events Δh_{UC} and Δh_{LC} must add up to match Δh (predicted in Fig. 2B, and in the previous section of the text). Assuming these variations occur on wavelengths shorter than the flexural wavelength of the lithosphere (Fig. 2A), the fluctuation in extrusive thickness will lead to little or no downward flexing of the lithosphere, and result in seafloor topographic variations of amplitudes equivalent to Δh_{UC}. Δh_{UC} can therefore be used as an upper-bound for the topography fluctuation due to extrusive processes.

Fault spacing set by tectono-magmatic interactions:

Let us consider the simple cycle of fault initiation, growth and abandonment illustrated in Fig. 3B. In a time-averaged sense, a fraction M of total plate separation at the ridge axis is accommodated magmatically by the emplacement of new oceanic crust. The remaining fraction (1-M) is accommodated by slip on normal faults that initiate near the axis, where the oceanic lithosphere is thinnest (*24*). Magmatic intrusion at the axis pushes each newly formed fault away from the axis where it encounters thicker and thicker lithosphere (Fig. 3B, top panel). This increases the mechanical cost of sustaining slip on the active fault, because as the fault cuts through a thicker brittle layer, a greater force is required to a) keep the fault at its failure point, b) flex the adjacent footwall and hanging wall blocks and c) sustain the growth of topography (*25*, *34-37*). At some point, it becomes mechanically favorable to break a new fault at the ridge axis than to sustain slip on the active fault (Fig. 3B, bottom panel).

Each of these forces can be estimated following the approach of ref. *25*. In a lithosphere of thickness H, with friction coefficient μ = 0.6 and cohesion C = *30* MPa, the force required to break a fault of dip θ writes

$$F_I = \frac{\mu \rho_m g H^2 / 2 + HC}{\mu \sin^2\theta + \sin\theta\cos\theta}. \quad (12)$$

For simplicity, we assume that all faults initiate at a dip of 55º, and instantly become cohesionless. As they accumulate horizontal offset ξ, they induce flexure in the footwall and hanging wall blocks, which causes them to rotate to a shallower angle (*37*, *38*). We assume a rotation of five degrees per kilometer of horizontal offset, until the fault reaches a minimum dip of 35º (*25*). The force required to keep the fault active therefore evolves with increasing offset:

$$F_F = \frac{\mu \rho_m g H^2(\xi) / 2}{\mu \sin^2\left(\theta(\xi)\right) + \sin\left(\theta(\xi)\right)\cos\left(\theta(\xi)\right)}. \quad (13)$$

The $H^2(\xi)$ term in Equation 13 expresses the fact that as the fault grows and migrates off-axis it encounters thicker and thicker lithosphere (Fig. 3B). The other mechanical cost of fault growth pertains to the flexure of the adjacent blocks, and the development of seafloor topography. This can be parameterized into a single force term, which increases with increasing offset:

$$F_B = AH^2(\xi)\left(1 - e^{-B\xi/H(\xi)}\right). \quad (14)$$

In Equation 14, A and B denote constants calibrated against numerical models of faulting in elasto-plastic lithosphere (*36*), here set to 5000 Pa/m and 50, respectively (*25*). The maximum heave h_{MAX} on a fault can therefore be estimated by finding the value of ξ at which (F_F + F_B) starts exceeding F_I. Fig. S1 illustrates this increase in force with increasing horizontal offset in a lithosphere that is 1.9 km thick at the ridge axis and doubles in thickness ~3 km off-axis. This force increase is strongly modulated by the rate of magma emplacement at the axis (M), which sets the rate at which H increases with ξ. Once h_{MAX} is known, the characteristic spacing S between successive faults can be obtained through:

$$S = \frac{M}{1-M} h_{MAX} \quad (15)$$

The MATLAB® script used to do this is provided as part of Materials section below. This code calculates h_{MAX}, S, and the maximum distance of off-axis fault migration for a given value of M, axial lithospheric thickness H_0, and rate of off-axis lithosphere thickening dH/dx.

In the main text we apply this theoretical framework to the problem of abyssal hill spacing vs. spreading rate. To do so requires estimates of M, H_0 and dH/dx vs. spreading half-rate U. At slow-spreading ridges, the fraction of magmatic extension M varies temporally and spatially at the segment scale, and values between ~0.3 and ~0.8 account for the diversity of fault morphologies (*24*, *25*, *39*, *40*). At intermediate- and fast-spreading ridges, magma supply is generally more robust and continuous, and values of 0.7–0.95 can be expected (*24*). We construct three empirical M vs. U curves capturing this basic trend. These bound estimates of M obtained from summing the throws of major faults to quantify the fraction of tectonic extension along selected cross-axis bathymetric profiles (*25*), shown in the inset of Fig. 3A, and in Fig. S2B. The orange and green curves are upper and lower bounds on M, respectively, each predicting different S vs. U curves in Fig. 3A and S2A. The red curve is an intermediate estimate.

The thickness of the oceanic lithosphere at the ridge axis H_0 decreases systematically with increasing spreading rate (*14*, *41*). The depth of seismically imaged axial magma lenses constitutes an excellent proxy for axial thickness, as the roof of these magma bodies generally coincides with the brittle-ductile transition at a MOR axis. We construct an upper envelope for H_0 as a function of spreading rate using compiled AML depth data (*20*) (Fig. S2C). In addition, to avoid further complexity and limit the number of free parameters, we assume a rate of off-axis thickening ($\phi = \tan^{-1} dH/dx$) of 30º at all spreading rates, as this parameter does not seem to affect the results as strongly as M and H_0.

Numerical models of fault growth interacting with intermittent magma supply:

To investigate the sensitivity of topography to tectono-magmatic interactions with rapid fluctuations in melt supply, we conducted 2-D numerical simulations of magmatic injection and fault growth at an intermediate-spreading ridge (*27*). We used FLAC, an explicit hybrid finite-element / finite-difference technique (*42*) adapted to model extensional environments (*36, 43*) in order to solve for conservation of mass, momentum and energy in a 60×15 km domain consisting of a brittle lithosphere overlying a ductile asthenosphere (Fig. S3A). The domain is subjected to horizontal extension at a half-rate

of 3 cm/yr applied symmetrically on the side boundaries. The top boundary has zero traction and the bottom is subject to lithostatic normal stress and no shear stress. Both are free to deform with the Lagrangian grid, which is periodically re-interpolated to a new regular, rectilinear grid to avoid excessive distortion. The material deforms according to a dry diabase flow law (*44*), which ensures that the shallow region that is cooler than ~600ºC (lithosphere) behaves elasto-plastically, while the hotter areas behave visco-elastically. The shear modulus and Poisson's ratio of the material are set to 30 GPa and 0.25, respectively. The non-Newtonian power law of ref. *44* provides an acceptable approximation for the viscous rheology of both the oceanic crust and the underlying mantle (*25*, *28*, *39*), thereby eliminating the need to keep track of crust and mantle units. Since the brittle-ductile transition roughly coincides with the 600ºC isotherm in this flow law, the geometry of the lithosphere evolves with the thermal structure. The temperature (advection-diffusion) equation is solved using Dirichlet boundary conditions on the top and bottom (T = 0 and 1300ºC, respectively), and no heat flux through the sides. The only heat source term we considered is associated with magma injection at the ridge axis, in the middle of the domain (see below). In all simulations, a steady-state thermal structure is rapidly attained (Fig. S3B), in which the 600ºC isotherm thickens off-axis at a rate determined by the extension rate and the thermal diffusivity of the material (8×10^{-7} m^2/s). We locally enhance the thermal diffusivity by a multiplying factor that varies spatially between 6 and 12 in the shallow (brittle) portion of the domain to simulate the effect of advective heat loss by hydrothermal circulation (*28*). This allows the axial lithosphere to retain a thickness of ~2 km as it extends.

A Mohr-Coulomb failure criterion is implemented in the lithosphere, assuming a friction coefficient of 0.6 and material cohesion of 44 MPa in intact (unyielded) material (*36*). Wherever this criterion is met, the material weakens so that the stresses are capped at the failure envelope. To favor strain localization, cohesion is weakened linearly with accumulated plastic strain until the plastic strain reaches a critical value of 0.3, at which point cohesion reaches a minimum of 2 MPa. This leads to the spontaneous development of plastic shear bands, which represent fault zones that are typically ~4 element wide. This class of models therefore yields mesh-dependent solutions, but is known to produce consistent shear band behavior provided the grid resolution is sufficient (*36*, *43*). To promote the formation of narrow shear bands, the model resolution is increased near the ridge axis, with ~200-m wide elements. The amount of fault slip necessary for full fault weakening is thus ~240 m (*36*). In addition, a healing mechanism is implemented such that the accumulated plastic strain decreases exponentially over a characteristic time scale (5×10^{12} s) wherever yielding ceases to occur (*43*).

Magmatic injection at a rate equal to the full plate separation can be imposed periodically in an injection zone that is 8-element wide (1.6 km) and spans the entire thickness of the lithosphere at the axis. This is done by allowing the injection zone to widen in a manner that relieves all deviatoric tension within the zone (*28*). Whenever magmatic injection is active, a heat source term and a modified diffusivity term accounting for the emplacement of hot, crystallizing material is added to the temperature equation following the parameterization of ref. *25*. Finally, the material viscosity within the injection zone is capped at a maximum value of 10^{19} Pa·s, as is done in certain simulations from ref. *28*. This constraint allows the development of a pronounced axial high by enabling the axial region to rise rapidly in periods of magmatic injection, due to

the buoyancy of the hot axial material (density of 3300 $kg.m^{-3}$ at 0ºC, with a coefficient of thermal expansion of 4.3×10^{-5} K^{-1}) (*28*). It does not affect the sequence of faulting.

Magmatic injection is explicitly cyclic. Each cycle contains a "magmatic phase" of duration $F_M \times \tau$ during which extension is accommodated entirely by magmatic injection. This phase is followed by a "tectonic phase" of duration $(1\text{-}F_M) \times \tau$, during which the magmatic injection is turned off and all the extension must be partitioned on faults. F_M sets the effective "long-term M" when averaged over many cycles. Here we set F_M to 0.85 to match estimates of M carried out at intermediate-spreading ridges (Fig. S2B). During amagmatic periods, plate separation can only be taken up on faults that form spontaneously on one side of the axis (Fig. S3B). During magmatic periods, however, faults are pushed off-axis by the emplacement of new material at the axis.

In addition to strain, stress and temperature fields, the model also outputs the topography of the top surface, which results from the successive growth of (almost) evenly spaced faults. Examples from a few runs are plotted in Fig. 4A. To compare the spectral content of this simulated bathymetry to observations (*6*), we computed the power density spectrum of profile a2, using the first 20 km to the right side of the axis (Fig. 4B). To remove trends inherited from long-wavelength features, we whitened this spectrum by multiplying it by wavenumber squared. We find that the strongest peak corresponds to fault spacing, and that multiple peaks with no straightforward interpretation exist in the 10-100 kyr period range.

Materials

Below is the MATLAB® script used to calculate the characteristic spacing of normal faults:

```
function [hmax,DS,xAF]=fault_heave_and_spacing(H0,dHdx,M)

% [hmax,DS,xAF]=fault_heave_and_spacing(H0,dHdx,M)
%
% this function gives the maximum heave (hmax), fault spacing (DS), and off-axis
% fault migration (xAF) that can be expected at a mid-ocean ridge
% characterized by an axial lithospheric thickness H0 thickening at a rate
% dHdx, where a fraction M of total plate separation is taken up by
% magmatic emplacement. Inputs and outputs in SI units.
%
% J.-A. Olive, August 2015, based on Behn and Ito [2008]

% PHYSICS
g=9.81;

% RHEOLOGY
% density
rho=3300; % density
% elasto-plastic parameters (Lavier et al., 2000)
A=5000; % Pa.m (5000 in B&I 2008, 1200 in Lavier et al. 2000)
B=50;
% failure criterion
mu=0.6; % friction coefficient
C0=30e6; % cohesion of unfaulted material (Pa)
% weakening
hcrit=0; % critical fault slip after which all cohesion is lost (m)
Cmin=4e6; % minimum cohesion

% fault heave
hmax=20; % km
N=10000;
h=linspace(0,hmax*1e3,N); % in meters
H=H0+dHdx*h*(M-0.5)./(1-M); % thickness of lithosphere "felt" by the fault

% fault rotation
dip0=55; % initial
ddipdh=5; % constant rotation rate from Behn and Ito, 2008
dipmin=35; % minimum
dip=max(dip0-ddipdh*h/1e3,dipmin*ones(size(h)));

% fault weakening
C=max(C0+(Cmin-C0)*h/hcrit,Cmin*ones(size(h)));

% forces
FB=A*H.^2.*(1-exp(-B*h./H));
FF=(mu*rho*g*H.^2/2+H.*C)./(mu*sind(dip).*sind(dip)+sind(dip).*cosd(dip));
FI=(mu*rho*g*H0.^2/2+H0.*C0)./(mu*sind(dip0).*sind(dip0)+sind(dip0).*cosd(dip0))*ones(siz
e(h));

DeltaF=FI-(FB+FF);

% max fault heave
hmax=max(h(DeltaF>=0));

% distance over which fault migrates off-axis
xAF=hmax*(M-0.5)./(1-M);

% fault spacing
DS=(M./(1-M)).*hmax;

end
```

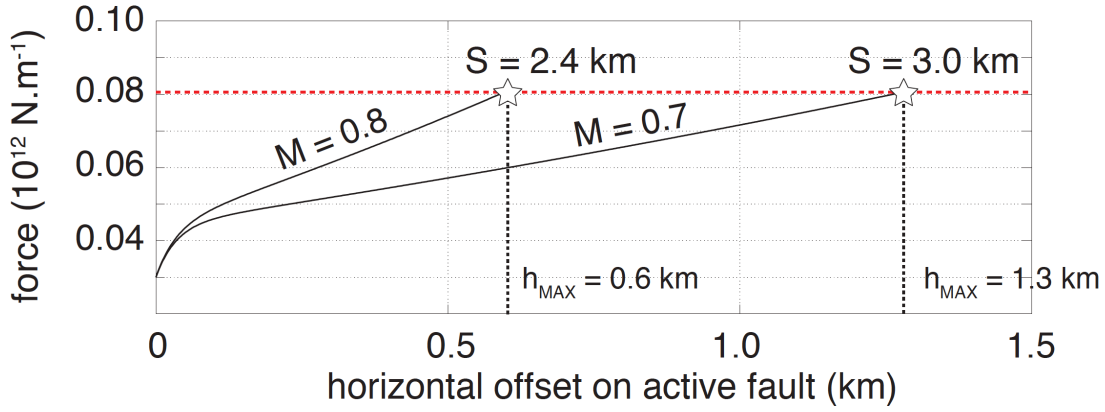

Fig. S1.

Force required to keep an fault at its failure point as it initiates in 1.9 km-thick lithosphere and migrates off-axis. The lithosphere is assumed to double in thickness over a distance of 3 km. Calculation assumes two different rates of magma injection (M = 0.7 and 0.8). The dashed red line indicates the strength of unfaulted (without strain weakening) lithosphere closer to the ridge axis. This is the threshold force where it becomes easier to break a new fault than to sustain slip on the initial fault.

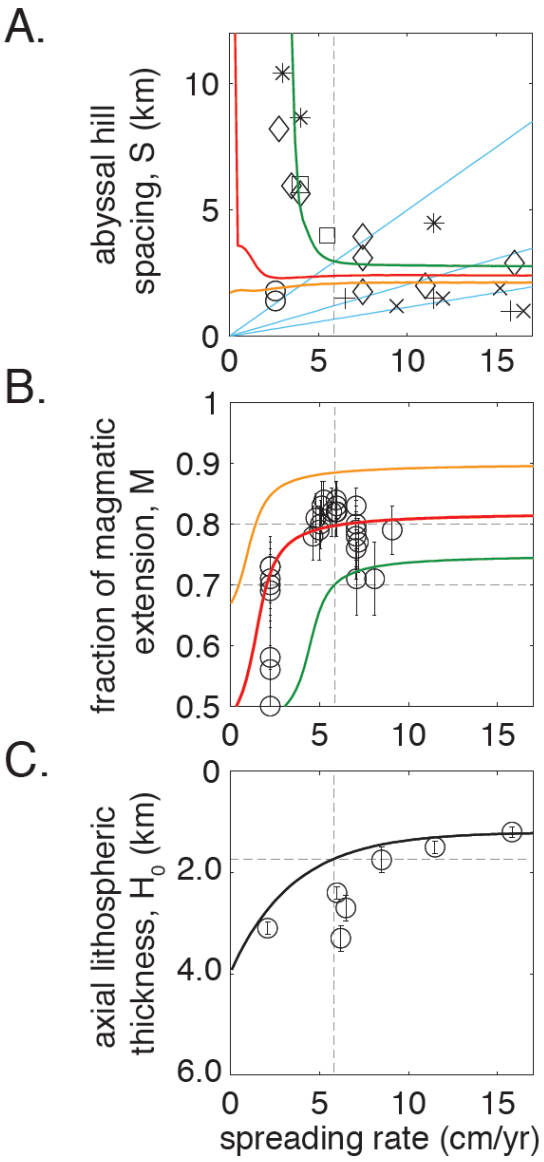

Fig. S2.

(A) Panel reproduced from Fig. 3A, for direct comparison with panels B and C. (**B)** Estimates of *M* at various mid-ocean ridges (circles, ref. *25*). The error bars indicate the full range of uncertainty in the determination of *M* from bathymetric profiles. The colored lines are three empirical parameterizations of M vs. spreading rate bounding the observations. (**C)** Depth to seismically imaged magma lenses at various ridges, with error bars indicating the full possible range (*20*). These depths provide an excellent, upper bound estimate for the axial thickness of the lithosphere H_0. The black line is an empirical parameterization providing a shallow-bounding envelope for the measured depths.

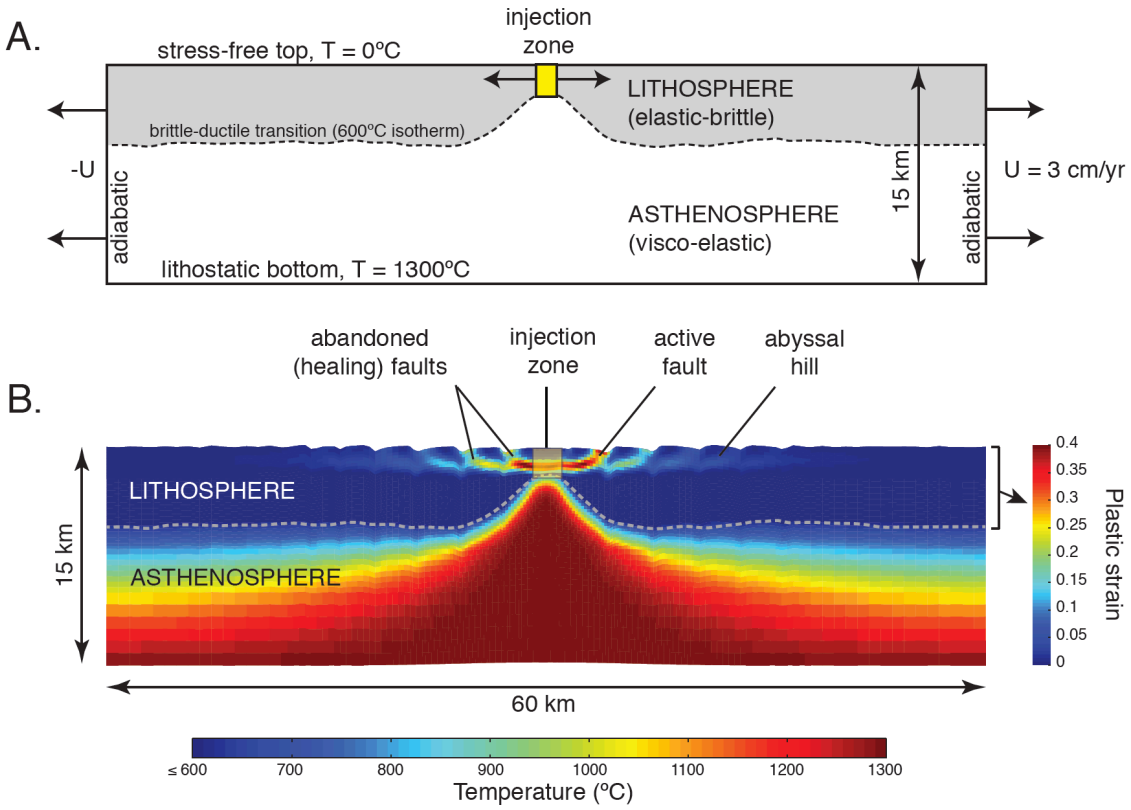

Fig. S3.

(A) Setup of the numerical model of fault growth with intermittent magmatic injection. (**B)** Snapshot of the simulation with tectono-magmatic period of τ = 50 kyr after 1.1 Myr of total extension, which produced profile a2 in Fig. 4A. The dashed gray line marks the brittle-ductile transition. In the ductile domain (asthenosphere), the color code indicates temperature, whereas in the brittle domain (lithosphere), it represents the accumulated plastic strain and reveals the location of active and abandoned faults.